nature climate change

SUPPLEMENTARY INFORMATION

DOI: 10.1038/NCLIMATE3157

In the format provided by the authors and unedited.

A re-examination of the projected subtropical precipitation decline

1. SPD over land and ocean

In this section we extend the analysis on the area of subtropical precipitation decline (SPD) over land and ocean. Table S1 extends Table 1 in the main text by showing results in all the coupled and AMIP simulations analyzed in this paper. Note that the AMIP_CO2 simulation projects a smaller fraction of robust decline and a larger fraction of robust increase over land compared to the other simulations, whereas the opposite is true for the AMIP_mean simulation.

Table S2 aims to verify the definition of robustness in Tables 1 and 1S by alternatively defining robustness as 85% or more model agreement (8 out of 9 models for 1pctCO2 and AMIP; 12 out of 13 for abrupt4xCO2) on the sign of precipitation change. It yields consistent results as Table S1.

Table S3 shows the area fraction of SPD that is projected over land in each individual model. Note that in the 1pctCO2 and sum of AMIP simulations, this fraction is less than 26.9% (which is the area fraction of the subtropics covered by land) for all models, although the difference is relatively small for HadGEM2-ES, IPSL-CM5B-LR, MPI-ESM-LR and MPI-ESM-MR. This indicates that models generally prefer SPD over ocean. However, this fraction becomes much larger in all models when the dynamic precipitation change from the AMIP_CO2 simulation is removed (rightmost column). This indicates that the land-sea warming contrast tends to offset the SPD over land.

Table S1. Area fraction of robust subtropical precipitation change for all coupled and AMIP simulations. This is the same as Table 1 in the main text except adding the abrupt4xCO2 and the individual AMIP simulations.

	Land % of robust $-\delta P$	Land % of robust $+\delta P$	% of land with robust $-\delta P$	% of land with robust $+\delta P$
abrupt4xCO2	20.4	32.3	11.2	20.6
1pctCO2	16.5	32.7	11.0	26.1
AMIP(total)	14.9	30.3	11.8	24.4
AMIP(total) - AMIP_CO2(dyn)	26.3	17.1	18.1	13.7
AMIP_CO2	8.8	92.5	18.4	32.8
AMIP_mean	54.1	12.8	24.0	20.2
AMIP_pattern	12.4	24.2	9.3	12.7

Table S2. Area fraction of robust subtropical precipitation change. This is the same as Table S1 in the main text except defining robustness as 85% or more model agreement (8 out of 9 models for 1pctCO2 and AMIP; 12 out of 13 for abrupt4xCO2) on the sign of precipitation change.

	Land % of robust $-\delta P$	Land % of robust $+\delta P$	% of land with robust $-\delta P$	% of land with robust $+\delta P$
abrupt4xCO2	20.6	31.1	10.1	18.9
1pctCO2	16.4	35.8	12.3	28.4
AMIP(total)	15.1	31.1	13.5	29.4
AMIP(total) - AMIP_CO2(dyn)	27.9	18.3	21.4	15.8
AMIP_CO2	9.2	91.4	19.9	39.3
AMIP_mean	54.5	13.1	28.2	21.2
AMIP_pattern	14.1	27.1	12.0	17.2

Table S3. Area fraction of SPD projected over land in each individual model. This is the same as the left first column in Tables 1, S1 and S2, except for each individual model.

Land % of robust –δP	1pctCO2	AMIP(total)	AMIP(total) - AMIP_CO2(dyn)
bcc-csm1-1	23.1	22.0	30.3
CanESM2	20.4	18.6	27.8
CNRM-CM5	19.0	18.9	25.8
HadGEM2-ES	26.1	22.8	29.3
IPSL-CM5B-LR	25.8	24.7	30.0
MIROC5	19.7	23.4	32.5
MPI-ESM-LR	26.6	22.7	28.7
MPI-ESM-MR	26.5	26.1	29.7
MRI-CGCM3	13.3	17.9	26.6

2. Precipitation and TS changes over time in the abrupt4xCO2 simulation

In the main text, we compare precipitation changes from the abrupt CO_2 forcing at year 1 and the end of the simulation. Because we only show one-year mean changes for the fast response (averaged for 13 models), internal variability may result in discrepancies among individual years, especially at regional scales. Here, we add more years to the comparison (Figure S1). Although the amplitude and pattern of SPD fluctuates in certain regions (e.g., the subtropical North Atlantic in year 1 and year 75), it is generally consistent over time. On the other hand, the precipitation decline in Southern Africa shows a steady growth over time and is therefore likely associated with the mean warming. As indicated by the stippling, almost all the colored signals exceed the amplitude of one standard deviation of internal variability estimated from the pre-industrial control simulation.

Note that the land-sea warming contrast and pattern of subtropical SST change also forms immediately after the CO_2 quadrupling (Fig. S2). The fast land warming in year 1 is close in amplitude to that in the AMIP_CO2 simulation (Fig. S3). The land-sea warming contrast persists over time. The initial land-sea warming contrast is largely due to difference in land-sea heat capacity but the final land-sea warming contrast is primarily related to the difference in land-sea relative humidity changes[1].

Although the land-sea warming contrast somewhat intensifies over time, the large-scale SPD does not. This indicates that the land-sea warming contrast might become less effective as the global mean SST increases. This could make sense – as the SST warms, moisture increases more over ocean relative to land, which acts to balance out the intensifying land-sea warming contrast (in terms of gross moisture stability change). The net result is that the mean SST warming increases precipitation over most of the subtropical oceans and reduces precipitation over most of the subtropical land (Fig. 3e in the main text). Likewise, the pattern of SST change also strengthens over time without substantially intensifying the SPD, particularly in the subtropical Southeast Pacific. This is largely due to the cancellation from the slow moistening over ocean driven by the mean SST warming (Fig. 3e in the main text).

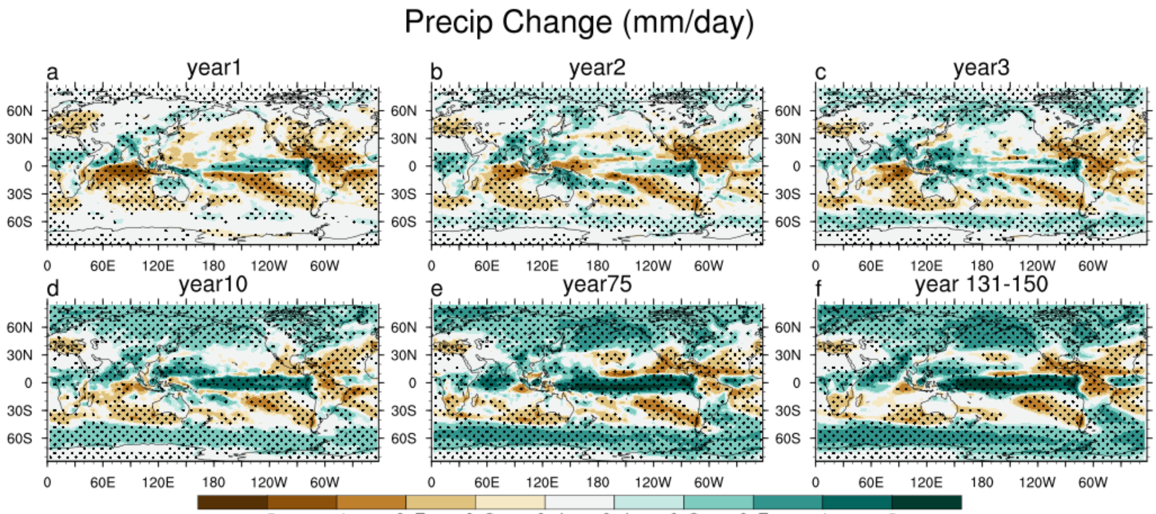

Figure S1. Ensemble mean time evolution of precipitation changes in the abrupt4xCO2 simulation. Regions where the amplitude of the ensemble mean change exceeds that of the inter-annual internal variability are stippled. The amplitude of the internal variability is estimated as the standard deviation of the ensemble mean yearly precipitation from the 100-year pre-industrial control simulation.

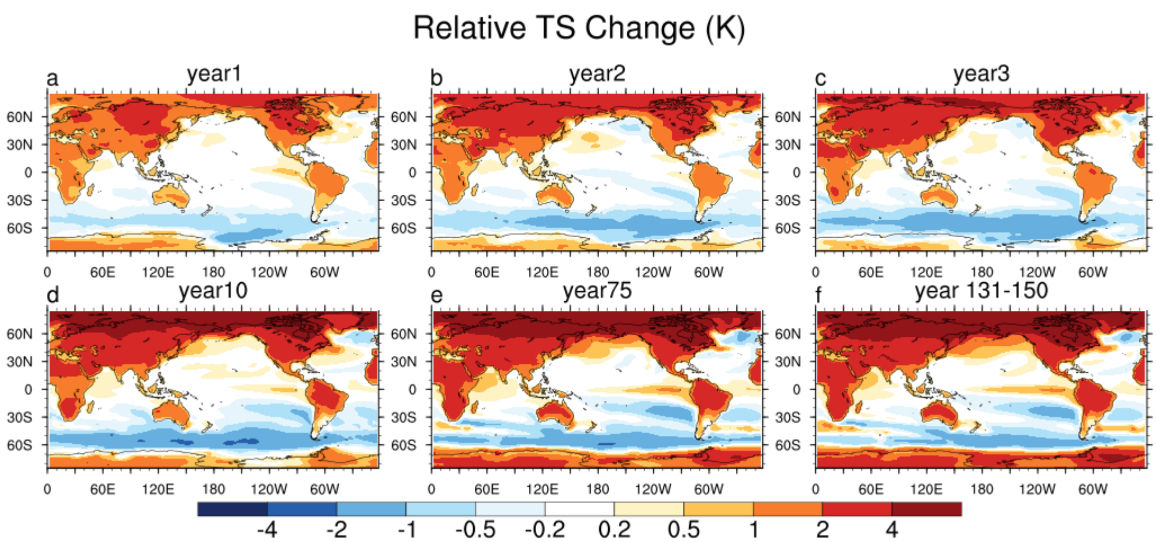

Figure S2. Ensemble mean time evolution of relative surface temperature changes in the abrupt4xCO2 simulation. This is the same as Figures S1, except for relative surface temperature change, which is calculated as the surface temperature change with the tropical mean sea surface temperature change removed.

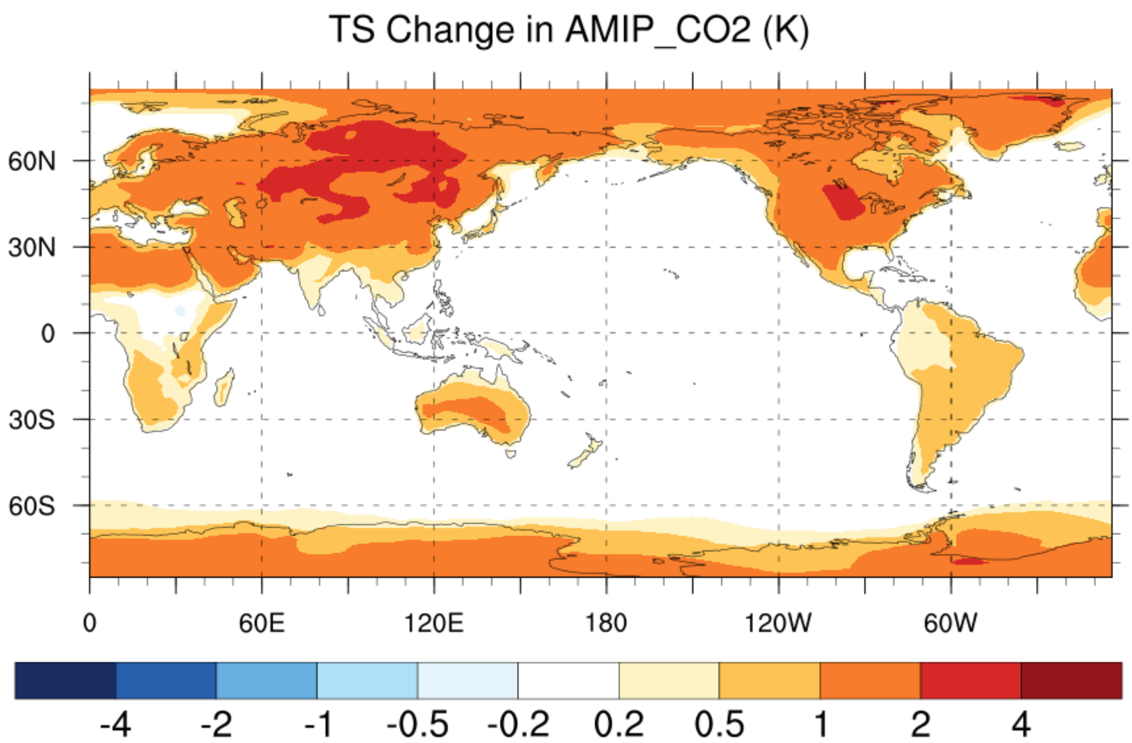

Figure S3. Ensemble mean changes in surface temperature from the AMIP_CO2 simulation. In order to compare with the fast surface temperature changes from abrupt4xCO2 (Fig. S2), results are not scaled or normalized (which is done for the rest of the paper as described in Method) and represent changes from 4xCO_2.

3. Mechanisms of changes in P – E

As shown in Figure S4a and S4b, changes in P – E generally follow a "wet-get-wetter and dry-get-drier" pattern over ocean, which is largely a response to the increase in moisture[2]. Because the increase in moisture is dominated by the mean SST warming, the large-scale changes in P – E are well reproduced in the AMIP_mean simulation (Fig. S4d). Discrepancies between Figure S4b and Figure S4d exist primarily in the deep tropics, where the pattern of SST change induces large changes in the hydrological cycle through changes in circulation (Fig. S4e).

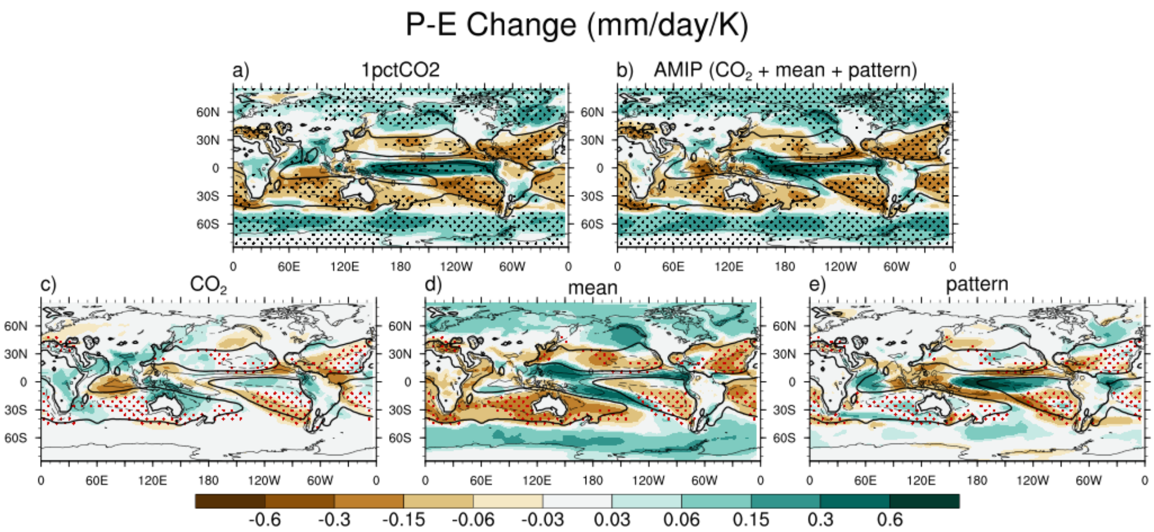

Figure S4. CMIP5 ensemble mean P – E changes. Same as Figure 3 in the main text except for changes in P – E.

4. The aquaplanet simulations

Figure S5 shows a comparison of the zonal mean P – E and precipitation between the 1pctCO2 and aquaplanet simulations. The changes in the aquaplanet simulations are calculated as the sum of the changes in aqua_CO2 and aqua_mean (Method). Because the maximum SST is prescribed at the equator, there is no double ITCZ in the aquaplanet simulations. Instead, the aquaplanet simulations show maximum precipitation climatology at the equator and a somewhat stronger Hadley cell than the one in the coupled simulation (Figs. S5a and S5b). In addition, the aquaplanet simulations show a much larger response at the Equator and a somewhat stronger response in the subtropics (Figs. S5c and S5d). Despite the differences in amplitude, the aquaplanet simulations have similar latitudinal positions of dry and wet zones and their corresponding changes.

As shown in Figure S6a, the SPD in the aquaplanet simulations is most pronounced between 30^o and 40^o latitude, which is similar to the latitudinal location of SPD in the 1pctCO2 simulation (Fig. 3 in main text). To be consistent with the coupled and AMIP simulations, we define the SPD regions of the aquaplanet simulations as the latitudinal bands between 10^o and 50^o latitude where the zonal mean precipitation change is negative.

As shown in the bar charts of Figure S6, the direct CO_2 forcing dominates the SPD, whereas the mean SST warming contributes to about one third of the total decline. In the aqua_mean simulation, the SPD is associated with a thermodynamic intensification of moisture export, a dynamic precipitation decline and a weakening in transient eddies. The former reflects the “dry-get-drier” mechanism, whereas the latter two are likely associated with the expansion of the Hadley cell (Fig. S8), as the SPD primarily occurs at the poleward edge of negative climatological P – E (contour in Fig. S6). These mechanisms are largely cancelled out by the increase in evaporation, yielding a relatively weak SPD.

Although the expansion of the Hadley cell appears to play a role in the SPD in the aquaplanet simulation, the results in the main text show that the bulk of the SPD in the coupled simulation is unrelated to the Hadley cell expansion. An crucial difference between the coupled and the aquaplanet simulations is that the two dominant drivers of SPD – the land-sea warming contrast and the pattern of SST change – only exist in the coupled simulation. Therefore, even if the Hadley cell expansion contributes to the SPD in the coupled experiment, it is relatively unimportant compared to its role in the aquaplanet simulation. In addition, we find that the dynamic precipitation change (averaged over the entire SPD) is positive in AMIP_mean (Fig. 4; albeit not robust among models), indicating that the Hadley cell expansion is not a key factor in the full GCMs even without land-sea warming contrast and pattern of SST change.

In the aqua_CO2 simulation, the SPD is primarily associated with the decrease in evaporation. In contrast to the AMIP_CO2 simulation, there is little dynamic change in the SPD regions. Note that both the AMIP_CO2[3] and the aqua_CO2 (Fig. S7) simulations show little expansion of the Hadley cell. However, the dynamic precipitation decline in the AMIP_CO2 simulation is primarily driven by the land-sea warming contrast, which does not exist in the aqua_CO2 simulation. In Section 6, we provide more analysis on the dynamic precipitation change in AMIP_CO2.

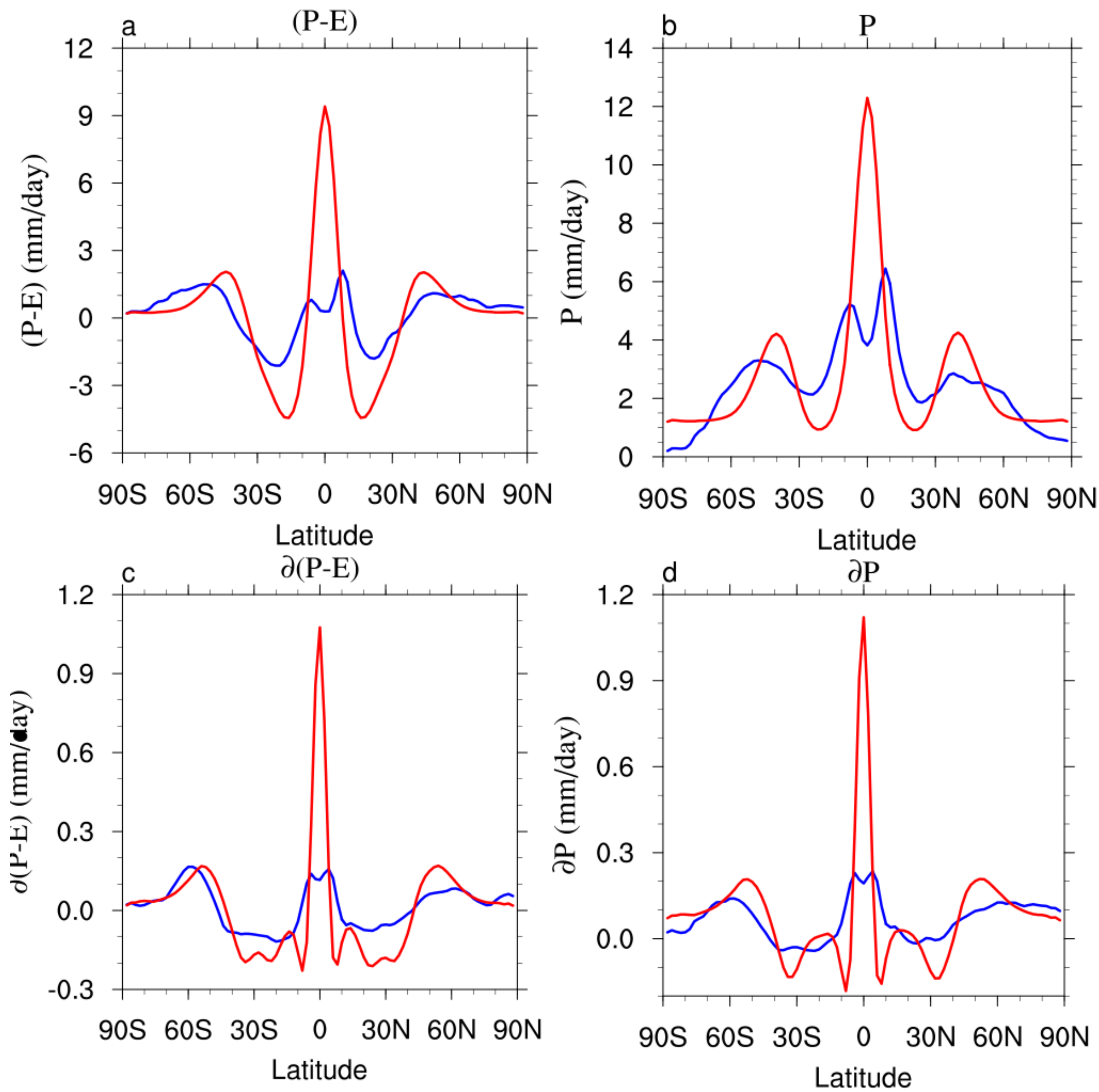

Figure S5. Zonal mean climatology and changes in P – E and precipitation. Blue lines represent the 1pctCO2 simulation, whereas red lines represent the aquaplanet simulations. All simulations use the same set of models (CNRM-CM5, MPI-ESM-LR, MPI-ESM-MR and MRI-CGCM3).

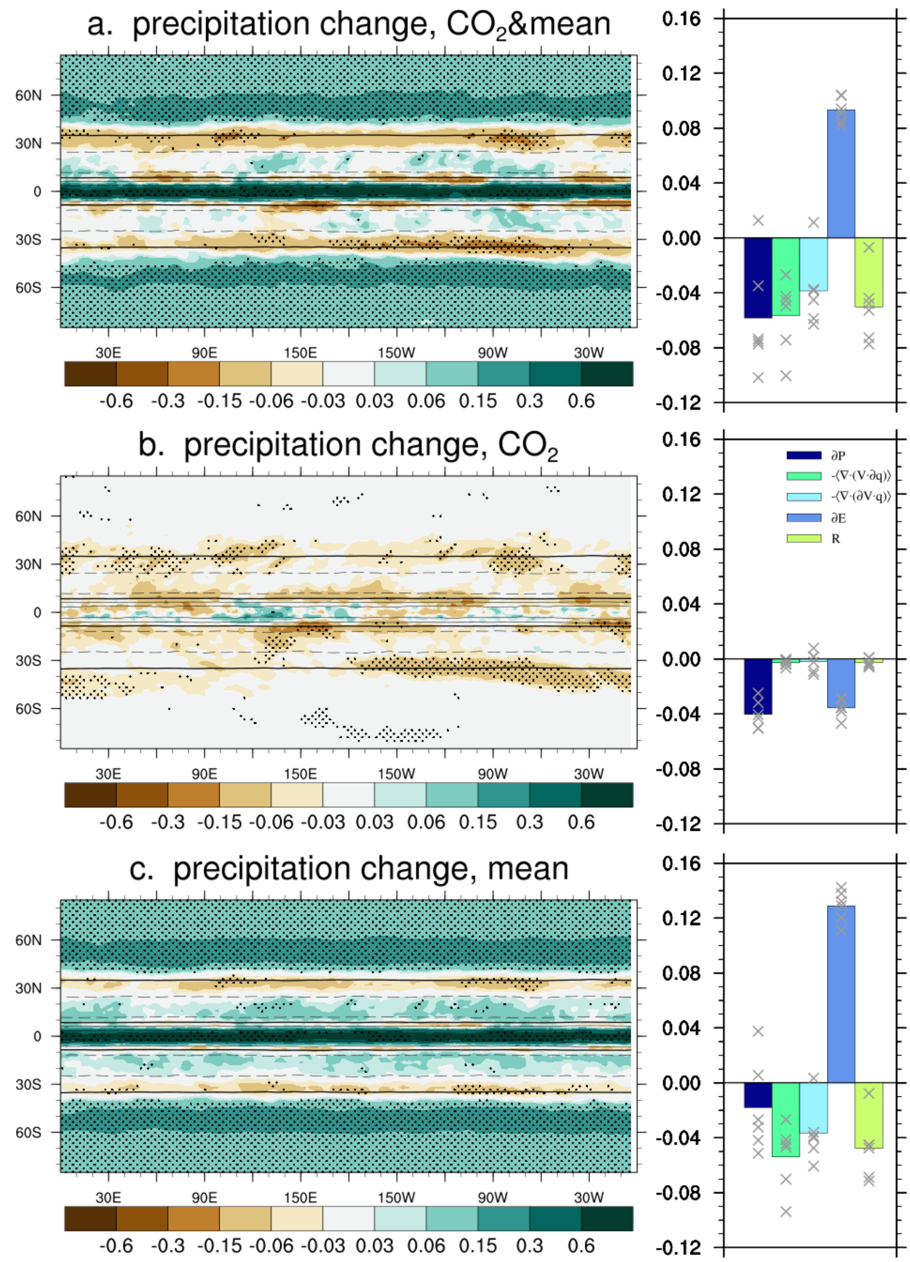

Figure S6. Ensemble mean changes in precipitation and moisture budget terms for SPD regions from the aquaplanet simulations. Top, middle and bottom panels are changes from the sum of aqua_CO2 and aqua_mean, aqua_CO2 and aqua_mean, respectively. Unit is mm/day/K. Contours in the left column show the climatological P – E taken from the aquaplanet control simulation. Contour interval is 3 mm/day. Zero contours are thickened. Dashed contours indicate negative values. The bar chart follows the same style as that in Figure 4 in the main text.

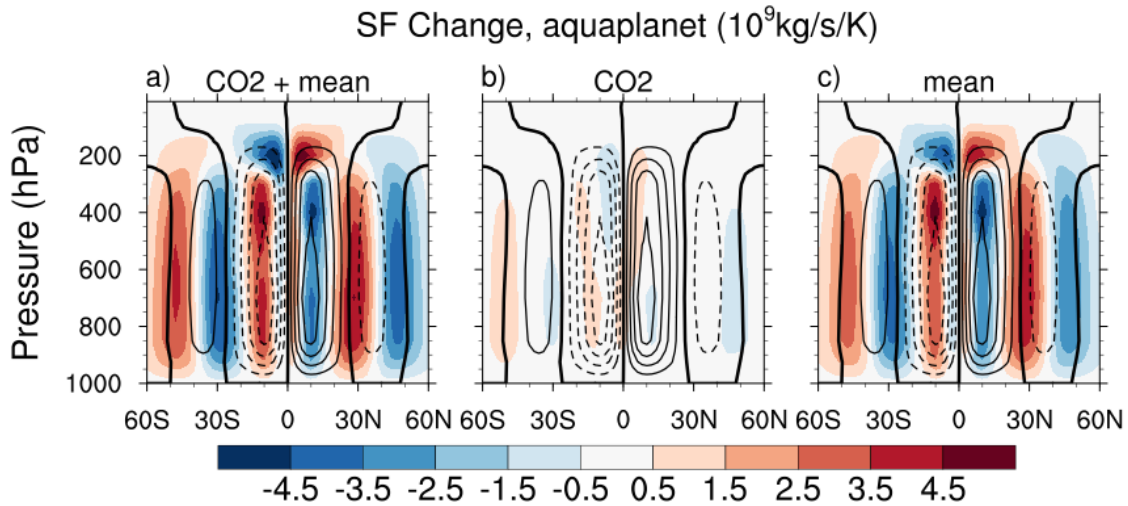

Figure S7. Ensemble mean changes in the zonal mean stream function from the aquaplanet simulations. Contours show the climatology of zonal mean stream function from the aquaplanet control simulation, following the same style as those in the middle column of Figure 1 in the main text.

5. Extended moisture budget analysis

The moisture budget analysis presented in Figure 4 (main text) uses partially different sets of models for the AMIP and aquaplanet simulations. In Figure S8, we show the analysis with the same set of models. The results are virtually identical to those in Figure 4.

In Figure S9, we present the moisture budget analysis for ocean and land separately. The total SPD is dominated by the ocean, whereas the land contribution is very small. (Note that the scale of the y-axis in the land panel is 1/6 of that in the ocean panel.) As a result, the moisture budget terms for the oceanic SPD regions are essentially the same as those for the entire SPD regions (Figure 4). The land SPD only occurs over small regions, namely the Mediterranean coast, the northwest tip of Mexico, southern Chile and southern Africa (Fig. 3b, main text). AMIP_mean dominates the total precipitation decline in these regions, whereas AMIP_pattern also contributes. The decline in the AMIP_mean simulation is primarily associated with the dynamic decline and the reduced evaporation and is weakly contributed by the thermodynamic decline. These terms are partially offset by the increase in the eddy transport term, which is consistent with the intensification of mid-latitude storm tracks[4].

The land thermodynamic decline is unusual due to the fact that the climatological P – E is almost always positive over land. Here, the thermodynamic decline only occurs over southern Chile (not shown). As discussed in ref 4, the moisture budget equation is relatively susceptible to errors in this region due to the sharp topography and the thermodynamic decline is likely a result of such error. The dynamic decline is consistent with the previous studies, which showed that the mean SST warming generally weakens convection over land[3,5]. The weakening of land convection can be attributed to the increased stability due to the enhanced deep convection over tropical oceans[6].

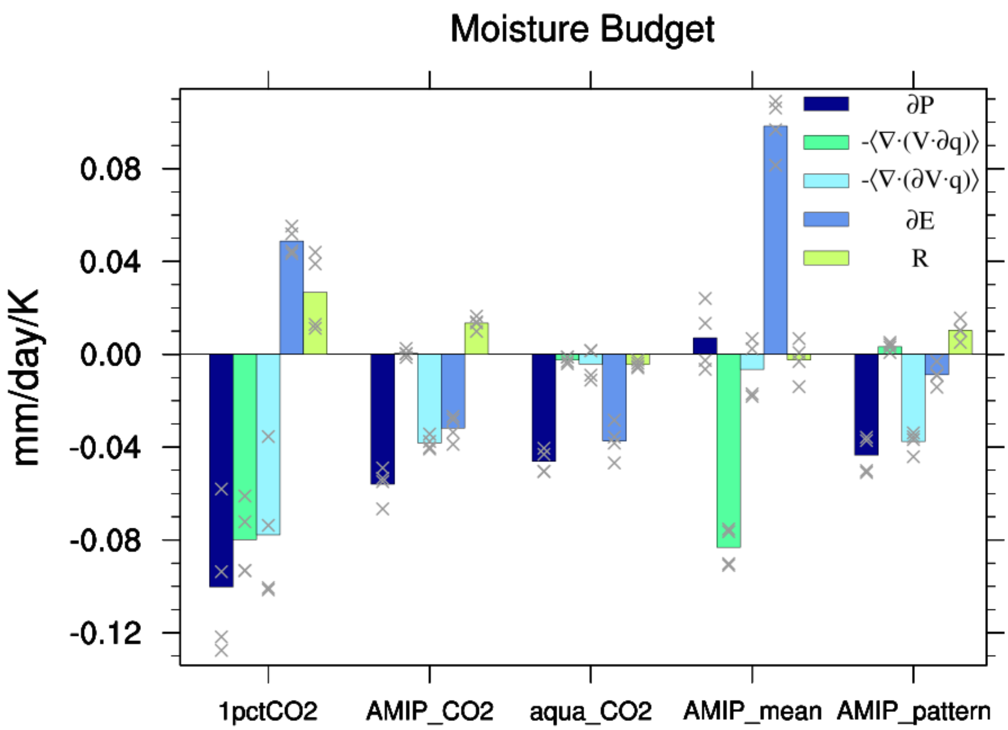

Figure S8. Changes in the moisture budget terms for SPD regions from the 1pctCO2, AMIP and aqua_CO2 simulations. This is the same as Figure 4 in the main text but using the same set of models (CNRM-CM5, MPI-ESM-LR, MPI-ESM-MR and MRI-CGCM3) for all simulations.

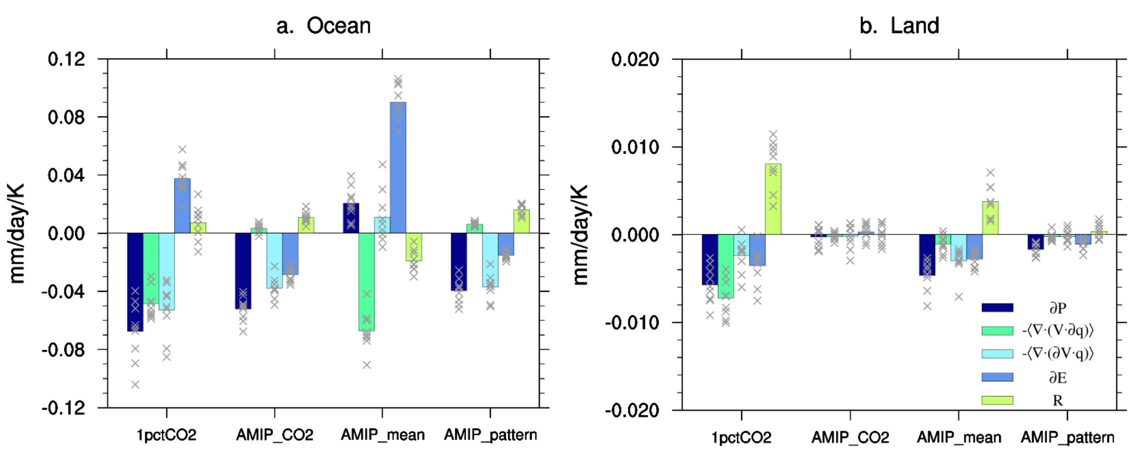

Figure S9. Changes in the moisture budget terms for the ocean and land SPD regions. The same as Figure 4 in the main text except that changes are summed over the ocean and land SPD regions separately and divided by the total area of the SPD regions.

6. Dynamic precipitation changes in AMIP_CO2

Figure S10 shows the decomposition of precipitation changes in the AMIP_CO2 simulation following the moisture budget analysis (Method). The dominant terms in the moisture budget equation are the dynamic term and the evaporation term. The evaporation term is negative over ocean and small over land. In general, the dynamic term increases precipitation over land with a magnitude similar to that of the dynamic precipitation decrease over ocean. This monsoon-like pattern indicates that the dynamic drying in the AMIP_CO2 simulation is likely driven by the land-sea warming contrast instead of the stabilizing effect of CO_2.

To further understand the mechanism of the dynamic precipitation change, we show its seasonal pattern in Figure S11. The increase of land precipitation occurs primarily in the summer hemisphere and equatorward of 40^o and appears to be associated with an enhancement of the existing low-level monsoon circulations and the resultant moisture convergence. In the adjacent oceanic regions, precipitation generally declines (e.g., the South Indian Ocean and the Southwest Atlantic Ocean in DJF and the North Indian Ocean in JJA). In some of the more remote oceanic regions, precipitation change exhibits a wave-train pattern (e.g., the southwest to northeast wave-train in the North Pacific in DJF, the zonal wave-train in the North Pacific and the meridional wave-train in the Southeast Pacific in JJA). A previous study of idealized monsoon experiments found that the subtropical monsoon heating generates Rossby waves, which act to strengthen the subtropical anticyclone by interacting with the mid-latitude westerlies[7]. A similar pattern of subtropical circulation response is indeed found in the AMIP_CO2 simulation, with intensified anticyclonic circulation over most of the subtropical oceans (Fig. S12). This remotely forced circulation response likely accounts for the SPD over the Southeast Pacific, the Northeast Pacific and the North Atlantic.

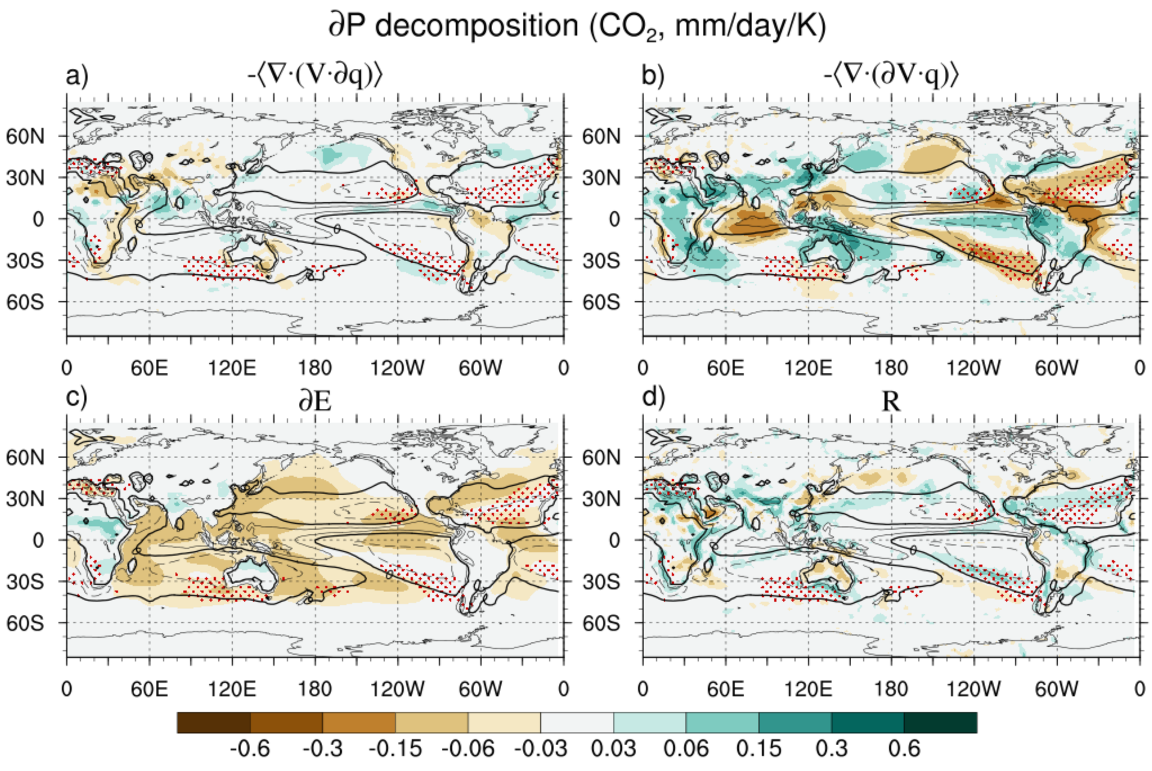

Figure S10. Changes in the moisture budget terms from the AMIP_CO2 simulation. Stippling follows the same style as that in Figure 3 in the main text. Contours show the climatological P – E, with an interval of 3 mm/day. Zero contours are thickened. Dashed contours indicate negative values.

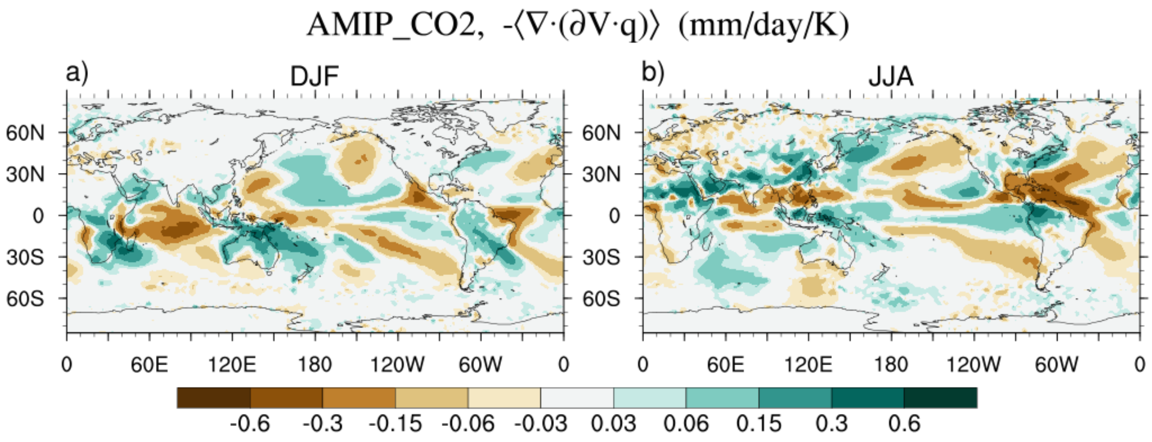

Figure S11. DJF and JJA dynamic precipitation change from the AMIP_CO2 simulation. This is the same as the shading in Figure S5b, except for DJF (right) and JJA (left).

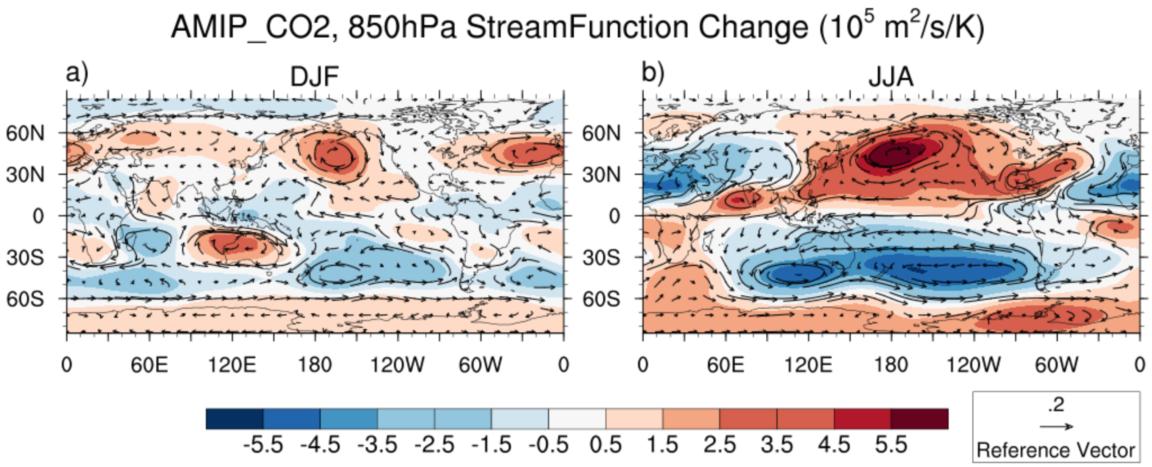

Figure S12. DJF and JJA changes in 850 hPa stream function (shading) and horizontal velocity (vector). The reference vector is 0.2 m/s/K.

7. Pattern of SST changes in the 1pctCO2 and AMIP_future simulations.

As shown in Figure S13, the pattern of SST changes is similar for the 1pctCO2 and AMIP_future simulations. Both show enhanced warming at the equatorial Pacific and equatorial Atlantic and reduced warming at certain subtropical oceans, including the Southeast Pacific, the Southeast Indian Ocean and the North Atlantic Ocean.

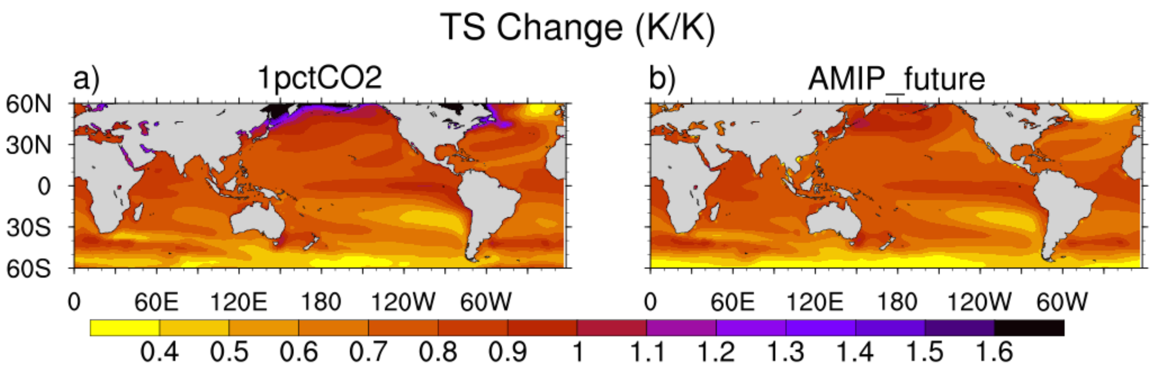

Figure S13. Ensemble mean changes in surface temperature from the 1pctCO2 and AMIP_future simulations. Changes are normalized by each model's global mean surface temperature as described in Method. Tropical (30^{o}S-30^{o}N) mean is 0.75K/K for 1pctCO2 and 0.74K/K for AMIP_future. The CMIP3 models used to calculate the pattern of SST changes for the AMIP_future simulation are: CCCma, CCSM3, CNRM-CM3, GFDL-CM2.0, GFDL-CM2.1, GISS-ER, INGV-SXG, inmcm3, IPSL-CM4, MIROC3.2-medres, MPI-OM, MRI-CGCM2.3.2, PCM and UKMO-HadGEM1.

References

1. Byrne, M. P. & O'Gorman, P. A. Link between land-ocean warming contrast and surface relative humidities in simulations with coupled climate models. *Geophys. Res. Lett.* **40,** 5223–5227 (2013).
2. Held, I. M. & Soden, B. J. Robust responses of the hydrological cycle to global warming. *J. Clim.* **19,** 5686–5699 (2006).
3. He, J. & Soden, B. J. Anthropogenic Weakening of the Tropical Circulation: The Relative Roles of Direct CO2 Forcing and Sea Surface Temperature Change. *J. Clim.* **28,** 8728–8742 (2015).
4. Seager, R., Naik, N. & Vecchi, G. A. Thermodynamic and dynamic mechanisms for large-scale changes in the hydrological cycle in response to global warming. *J. Clim.* **23,** 4651–4668 (2010).
5. Chadwick, R. Which Aspects of CO2 Forcing and SST Warming Cause Most Uncertainty in Projections of Tropical Rainfall Change over Land and Ocean? *J. Clim.* **29,** 2493–2509 (2016).
6. Giannini, A. Mechanisms of Climate Change in the Semiarid African Sahel: The Local View. *J. Clim.* **23,** 743–756 (2010).
7. Rodwell, M. J. & Hoskins, B. J. Subtropical Anticyclones and Summer Monsoons. *J. Clim.* **14,** 3192–3211 (2001).